
PERTURBED INITIAL ORBIT DETERMINATION

Alberto Fossà* 

Institut Supérieur de l'Aéronautique et de l'Espace
31055 Toulouse, France
alberto.fossa@isae-supaero.fr

Matteo Losacco† 

Institut Supérieur de l'Aéronautique et de l'Espace
31055 Toulouse, France
matteo.losacco2@isae-supaero.fr

Roberto Armellin‡ 

University of Auckland
1010 Auckland, New Zealand
roberto.armellin@auckland.ac.nz

ABSTRACT

An algorithm for robust initial orbit determination (IOD) under perturbed orbital dynamics is presented. By leveraging map inversion techniques defined in the algebra of Taylor polynomials, this tool is capable of not only returning an highly accurate solution to the IOD problem, but also estimating a range of validity for the aforementioned solution in which the true orbit state should lie. Automatic domain splitting is then used on top of the IOD routines to ensure the local truncation error introduced by a polynomial representation of the state estimate remains below a predefined threshold to meet the specified requirements in accuracy. The algorithm is adapted to three types of ground based sensors, namely range radars, Doppler-only radars and optical telescopes by taking into account their different constraints in terms of available measurements and sensor noise. Its improved performance with respect to a Keplerian based IOD solution is finally demonstrated with large scale numerical simulations over a subset of tracked objects in low Earth orbit.

Keywords Initial orbit determination · Range radar · Doppler radar · Optical telescope · Differential algebra

1 Introduction

An accurate characterization of the environment around the Earth is of paramount importance for all the operations required to ensure the safety of in-orbit missions, such as observation scheduling, collision risk assessment, and re-entry predictions. This characterization typically consists in estimating and updating the state and attitude of any active and inactive orbital object, and it can be performed only if the lasts are observed with enough accuracy and frequency. As a result, networks of ground-based and space-based optical, radar, and laser sensors are jointly used to monitor the near-Earth environment.

Nevertheless, the discrepancy between the objects that are regularly tracked and those predicted by mathematical models is significant. According to ESA's 2022 space debris environment report [1], around 36,500 space debris with size greater than 10 cm are estimated to exist. This number soars when considering smaller dimensions, with 1 million debris between 1 cm and 10 cm, and 130 million between 1 mm and 1 cm. Only around 33,640 objects are regularly tracked by the space surveillance networks and maintained in their catalogs. That is, existing catalogs currently cover just the larger-size portion of the orbiting population. Though the size and properties of the remaining objects prevent existing operational sensors from detecting or observing them with enough accuracy, the relentless launch activity and in-orbit generation events coupled with the constant technological improvements in modern sensors always offer the possibility of identifying and potentially characterizing uncatalogued objects.

*PhD Candidate, Department of Aerospace Vehicles Design and Control, 10 Avenue Edouard Belin.

†Postdoctoral Researcher, Department of Aerospace Vehicles Design and Control, 10 Avenue Edouard Belin.

‡Full Professor, Te Pūnaha Ātea - Space Institute, 20 Symonds Street.

Whenever an uncatalogued object is detected, an attempt to characterize its orbital state starting from the set of available measurements is performed. If the so-called initial orbit determination (IOD) process is successful, the object is associated with a state estimate, but not yet cataloged. New observations on subsequent passages will be required to refine this estimate before a new entry of the catalog is obtained. Methods to perform IOD can be generally divided according to the type of available measurements and the sensor that generates them. Three main categories of sensor exist, i.e. optical telescopes, range radars, and Doppler-only radars. Optical telescopes provide very accurate measurements of the angular position of the transiting object for each observation instant. The resulting so-called “angle-only” methods exploit this information to estimate the state of transiting object at one observation epoch. Classical examples of angle-only IOD methods are Laplace’s method [2], Gauss’ method [3], the double R iteration method [4], Baker-Jacobi’s method [5], Gooding’s method [6] and Karimi and Mortari’s methods [7]. Range radars are characterized by less precise angular measurements, but couple this information with the measurement of the object distance from the sensor, called slant range. Examples of classical “angle-range” IOD methods are Lambert’s method [8], Gibbs’ method [9], and Herrick-Gibbs’ method [10]. Doppler-only radars, instead, combine the angular information with the time derivative of the slant range. Examples of tailored IOD methods are the Doppler integration method (DIM) [11] and the hodograph method [12].

One limitation of the mentioned algorithms is the lack of information about the uncertainty on the provided state estimate, which is however of great importance for quantifying the accuracy of the obtained solution and perform data association to update the available catalogs. Recent IOD methods leveraged differential algebra (DA) techniques to overcome this problem by computing a polynomial expansion of the state estimate with respect to the uncertainties in the available measurements. Moreover, formulating the IOD problem in the DA framework eliminates the needs for an iterative procedure to solve for the object state, since polynomial map inversion is exploited to solve the implicit equations that arise from the problem formulation. Given the local validity of truncated Taylor series, the DA-based IOD methods must be coupled with the automatic domain splitting (ADS) algorithm [13] to control the truncation error introduced by a fixed expansion order. The final output is thus a manifold (i.e. set) of polynomials, each of them defined in a specific subdomain, whose union describes the uncertainty on the IOD estimate with the required accuracy. This family of methods, named DAIOD, were developed for all three kinds of ground-based sensors, i.e. optical telescopes [14], range radars [15] and Doppler-only radars [16], and constitute a compelling alternative to the more widespread IOD techniques cited above. Their advantages over these classical methods were in fact demonstrated in [14] by comparing the DAIOD and Gooding methods for angles-only IOD.

In order to obtain a solution, all methods previously cited resort to a simplified dynamical model, usually unperturbed Keplerian motion, that potentially reduce their range of applicability. Though generally valid for short-arc observations, this assumption no longer holds for longer arcs, and its introduction can affect the accuracy of both the orbital solution and its estimated uncertainty, with possible undesirable effects at a later stage during data association processes.

Starting from these considerations, this paper introduces three new IOD methods for angle-only, angle-range, and angle-range rate observations. The algorithms build on the mentioned DA-based IOD methods and extend them to a generic perturbed dynamics. The manuscript is structured as follows. Section 2 introduces the required mathematical background, namely DA, ADS and measurement regression. Section 3 illustrates the three methods for range radars (Section 3.1), Doppler-only radars (Section 3.2), and optical telescopes (Section 3.3). Finally, Section 4 illustrates the results of some numerical simulations, and shows a comparison between the proposed perturbed DAIOD methods and their Keplerian counterparts.

2 Mathematical background

The main mathematical tools on which the work is based are introduced in this section. They include DA with a focus on map inversion techniques, ADS for the control of the truncation error and a brief discussion on the dynamical model used to perform initial orbit determination.

2.1 Differential algebra

Differential algebra is a computing technique that stems from the idea that is possible to extract more information from a function f than its mere value $f(x)$ at a point x . Given any function $\mathbf{f} : \mathbb{R}^n \rightarrow \mathbb{R}^m$ that is \mathcal{C}^{k+1} in the domain of interest $\mathcal{D} = [-1, 1]^n$, the algebra of floating point numbers is replaced by a new algebra of Taylor polynomials to compute the k^{th} order expansion of \mathbf{f} [17]. The notation used in this paper is

$$\mathbf{f} \approx [\mathbf{f}] = \mathcal{T}_{\mathbf{f}}(\delta\mathbf{x}) \tag{1}$$

where $\delta\mathbf{x} = \{\delta x_1, \dots, \delta x_n\}^T$ are the n independent DA variables. When working with physical quantities \mathbf{x} , it is convenient to introduce some scaling factors β such that $\delta\mathbf{x} \in \mathcal{D}$. The domain of \mathbf{x} is then represented in the DA

framework by

$$[\mathbf{x}] = \bar{\mathbf{x}} + \boldsymbol{\beta} \odot \delta \mathbf{x} \quad (2)$$

where $\bar{\mathbf{x}}$ is the nominal value of \mathbf{x} , \odot denotes the Hadamard product, $\boldsymbol{\beta} \in \mathbb{R}_{\geq 0}^n$ and $\delta \mathbf{x} \in \mathcal{D}$. The parameters $\boldsymbol{\beta}$ may have different physical meaning. For instance, if \mathbf{x} is Gaussian distributed with mean $\bar{\mathbf{x}}$ and diagonal covariance $\boldsymbol{\Sigma} = \text{diag}(\sigma_i)$, β_i is commonly set equal to $3\sigma_i$ such that $[\mathbf{x}]$ represents a domain that spans three standard deviations around its mean $\bar{\mathbf{x}}$. In the specific case of IOD, values for $\boldsymbol{\beta}$ are given by either Eq. (21) or Eq. (22).

The four arithmetic operations, elementary functions (e.g. exponential, logarithm and trigonometric functions), derivation, integration, map composition and map inversion are all well defined in DA. These basic operations can be then combined to derive powerful algorithms for the solution of implicit equations, the computation of the flow of the dynamics in terms of their initial conditions [18] and the solution of boundary value problems [19].

2.1.1 Map inversion

Suppose that the k^{th} -order Taylor expansion of \mathbf{y} in terms of $\delta \mathbf{x}$ is known as $[\mathbf{y}] = \mathcal{T}_{\mathbf{y}}(\delta \mathbf{x})$, but an explicit expression for its inverse is needed instead. This problem can be efficiently solved in the DA framework with a simple fixed-point iteration scheme [17]. The polynomial $\mathcal{T}_{\mathbf{y}}(\delta \mathbf{x})$ is firstly split into its constant part and non-constant part as

$$\mathcal{T}_{\mathbf{y}}(\delta \mathbf{x}) = \bar{\mathbf{y}} + \mathcal{T}_{\delta \mathbf{y}}(\delta \mathbf{x}) \quad (3)$$

Then, the map $\delta \mathbf{y} = \mathcal{T}_{\delta \mathbf{y}}(\delta \mathbf{x})$ is inverted as follows. Its polynomial expansion is further separated into its linear part and non-linear part as

$$\mathcal{T}_{\delta \mathbf{y}} = M_{\delta \mathbf{y}} + \mathcal{N}_{\delta \mathbf{y}} \quad (4)$$

where the dependency on $\delta \mathbf{x}$ has been dropped for clarity. It is then observed that

$$\mathcal{T}_{\delta \mathbf{y}} \circ \mathcal{T}_{\delta \mathbf{y}}^{-1} = \mathcal{I} \quad (5)$$

with \mathcal{I} the identity map, $\mathcal{T}_{\delta \mathbf{y}}^{-1}$ the inverse map and \circ denoting map composition. A fixed-point scheme can be then setup as

$$\mathcal{T}_{\delta \mathbf{y}}^{-1} = M_{\delta \mathbf{y}}^{-1} \circ \left(\mathcal{I} - \mathcal{N}_{\delta \mathbf{y}} \circ \mathcal{T}_{\delta \mathbf{y}}^{-1} \right) \quad (6)$$

the inverse map is guaranteed to exist if $M_{\delta \mathbf{y}}$ is invertible, in which case Eq. (6) converges in exactly k steps where k is the expansion order. The Taylor expansion of $\delta \mathbf{x}$ is finally available as

$$\delta \mathbf{x} = \mathcal{T}_{\delta \mathbf{x}}(\delta \mathbf{y}) = \mathcal{T}_{\delta \mathbf{y}}^{-1}(\delta \mathbf{y}) \quad (7)$$

This algorithm is heavily used in Section 3 to compute a correction to the IOD solution that guarantees a continuous trajectory in the perturbed dynamical model of choice.

2.2 Automatic domain splitting

Taylor polynomials are only a local approximation of the function \mathbf{f} around its expansion point $\bar{\mathbf{x}}$, and the accuracy of the DA map $\mathcal{T}_{\mathbf{y}}(\delta \mathbf{x})$ drops while moving farther from $\bar{\mathbf{x}}$. Given the domain of interest for $\delta \mathbf{x}$, usually $\delta \mathbf{x} \in [-1, 1]^n$, the objective is to keep the truncation error across the entire domain below a predefined threshold. This can be achieved by either increasing the expansion order k or, for a fixed order, reducing the size of the domain for a single expansion and patching several polynomials to cover the initial domain. Since the number of polynomial coefficients grows exponentially with k , increasing the expansion order becomes computationally intractable above a certain threshold. The second idea was thus formalized in [13] with the development of an algorithm for the automatic control of the truncation error of Taylor expansions. This technique, named automatic domain splitting (ADS), monitors the accuracy of $\mathcal{T}_{\mathbf{y}}(\delta \mathbf{x})$ by estimating the magnitude of the coefficients of order $k + 1$ and splits the initial domains into two smaller ones as soon as the estimated coefficients grow above a predefined threshold. This operation is carried out recursively for each subdomain until each map is deemed sufficiently accurate in its domain of interest. Starting from a single polynomial $[\mathbf{x}]$ and a function \mathbf{f} to be evaluated, the procedure generates two sets of polynomials, or manifolds, for both the domain and its image through \mathbf{f} , defined as

$$M_{\mathbf{x}} = \left\{ [\mathbf{x}^{(i)}] : \bigcup_{i=1}^N [\mathbf{x}^{(i)}] = [\mathbf{x}] \right\} \quad (8a)$$

$$M_{\mathbf{y}} = \left\{ [\mathbf{y}^{(i)}] : \bigcup_{i=1}^N [\mathbf{y}^{(i)}] = [\mathbf{y}] \right\} \quad (8b)$$

where $[\mathbf{y}] = \mathbf{f}([\mathbf{x}])$ and N is the total number of subdomains generated by the algorithm.

2.3 Measurements regression

Ground sensors usually provide multiple measurements of the target space object (SO) taken at different epochs within the same observation window. The developed IOD algorithms, however, use at most three instants to estimate the object's state. To maximize the information that is conveyed from the raw measurements to the IOD solution, a preprocessing of the sensor data can be performed. Each observable is treated as an independent Gaussian random variable and polynomial regression is employed to estimate the observed quantities and corresponding confidence intervals (CIs) at the epochs required by the IOD algorithms [14], [16].

Consider a set of N measurements for the generic observable Y , where each entry is normally distributed and characterized by its mean value y_i and standard deviation σ_i . This set is denoted as

$$\{t_i; (y_i, \sigma_i)\} \quad i \in [1, N] \quad (9)$$

with t_i the observation epoch and $Y_i \sim \mathcal{N}(y_i, \sigma_i)$ the independent random variable at t_i . A least squares (LS) problem is then set up to fit the observed data and obtain the $m + 1$ coefficients that model a polynomial dependency between the observation epoch and the observed measurements. The design matrix is firstly built as

$$A = \begin{bmatrix} 1 & t_1 - t_0 & \dots & (t_1 - t_0)^m \\ \vdots & \vdots & \ddots & \vdots \\ 1 & t_N - t_0 & \dots & (t_N - t_0)^m \end{bmatrix} \quad (10)$$

where t_0 is the regression epoch, here selected as the epoch t_i closest to the middle of the observation window, and $m \in [1, N - 2]$ is the regression order. The LS problem is then given by

$$\mathbf{y} = A\mathbf{z} \quad (11)$$

with $\mathbf{y} = \{y_1, \dots, y_m\}^T$ the real observations and $\mathbf{z} = \{z_0, \dots, z_m\}^T$ the regression parameters. If available, prior information on the measurements uncertainty can be taken into account in the solution of Eq. (11) by introducing a weight matrix $W = \text{diag}(1/\sigma_i^2)$ where σ_i are the measurements' standard deviations. The solution to the weighted least squares problem is then obtained as

$$\hat{\mathbf{z}} = (A^T W A)^{-1} A^T W \mathbf{y} \quad (12)$$

while the estimated measurements $\hat{\mathbf{y}}$ are given by

$$\hat{\mathbf{y}} = A\hat{\mathbf{z}} \quad (13)$$

Finally, the covariance matrices of the estimated parameters $\hat{\mathbf{z}}$ and measurements $\hat{\mathbf{y}}$ are computed as

$$P_{\hat{\mathbf{z}}\hat{\mathbf{z}}} = (A^T W A)^{-1} \quad (14a)$$

$$P_{\hat{\mathbf{y}}\hat{\mathbf{y}}} = A P_{\hat{\mathbf{z}}\hat{\mathbf{z}}} A^T \quad (14b)$$

If no prior information on the measurement uncertainty is available, the solution is instead obtained as

$$\hat{\mathbf{z}} = (A^T A)^{-1} A^T \mathbf{y} \quad (15)$$

while the estimated measurements $\hat{\mathbf{y}}$ are still given by Eq. (13). An estimate for the measurements uncertainty is then computed as

$$\hat{\sigma}^2 = \frac{\hat{\mathbf{r}}^T \hat{\mathbf{r}}}{N - p} \quad (16)$$

with $\hat{\mathbf{r}} = \mathbf{y} - \hat{\mathbf{y}}$ the measurements residuals and $p = m + 1$. The covariance matrix of the fitted parameters is now obtained as

$$P_{\hat{\mathbf{z}}\hat{\mathbf{z}}} = \hat{\sigma}^2 (A^T A)^{-1} \quad (17)$$

while $P_{\hat{\mathbf{y}}\hat{\mathbf{y}}}$ is still given by Eq. (14b). If the hypothesis of independence between measurements holds, it can be shown that

$$\frac{\hat{y}_i - y_i}{\sqrt{P_{\hat{\mathbf{y}}\hat{\mathbf{y}}, ii}}} \sim t_{N-p} \quad (18)$$

where t_{N-p} denotes the student's t-distribution with $N - p$ degrees of freedom. An estimate for the CI of the i^{th} observation is then obtained as

$$\text{CI}_{\hat{y}_i} = \left[\hat{y}_i \pm q_{\frac{1+\alpha}{2}, N-p} \cdot \sqrt{P_{\hat{\mathbf{y}}\hat{\mathbf{y}}, ii}} \right] = [\hat{y}_i \pm \Delta \text{CI}_{\hat{y}_i}] \quad (19)$$

where α is the confidence level and $q_{\frac{1+\alpha}{2}, N-p}$ is the quantile function (or inverse cumulative distribution function) of t_{N-p} evaluated at $\frac{1+\alpha}{2}$. The CI is thus the interval within which the true value can be found with a confidence level α .

The developed IOD algorithm requires the input measurements being initialized as DA variables to obtain a polynomial representation of their nominal values and associated uncertainties. In the DA framework these are denoted as

$$[y_i] = \bar{y}_i + \beta_{y_i} \delta y_i \quad (20)$$

where \bar{y}_i is the nominal value, δy_i the first-order deviation in y_i and $\beta_{y_i} \in \mathbb{R}_{\geq 0}$ a scaling coefficient for the measurement uncertainty. If measurements regression is performed, Eq. (20) is rewritten as

$$[y_i] = \hat{y}_i + \Delta \text{CI}_{\hat{y}_i} \cdot \delta y_i \quad (21)$$

where \hat{y}_i and $\Delta \text{CI}_{\hat{y}_i}$ are the estimated measurements and associated confidence intervals given by Eqs. (13) and (19) respectively. These values are the result of a polynomial regression and are thus dependent on the control parameters m and α . In particular, lower regression orders m and larger confidence levels α will result in larger $\Delta \text{CI}_{\hat{y}_i}$ which are more likely to include the true, yet unknown, measurement. At the same time, larger confidence intervals may trigger more splits when solving the IOD problem within the ADS framework. The two parameters have thus to be chosen for the best trade-off between accuracy, quantified by the likelihood of including the true measurements within the DA variables bounds, and computational effort, quantified by the number of domains generated by the ADS algorithm.

If raw observations are used instead, $[y_i]$ is initialized as

$$[y_i] = y_i + 3\sigma_i \cdot \delta y_i \quad (22)$$

where y_i and σ_i are the measurement's mean and standard deviation given by Eq. (9).

2.4 Dynamical models

The IOD algorithms developed in Section 3 start by computing a nominal solution to the IOD problem under the assumption of unperturbed Keplerian motion. The latter is then refined in an higher fidelity dynamical model to compensate for the deviations from the nominal two-body trajectory, which might be non negligible for long observations windows, and to compute a polynomial expansion of the solution with respect to measurements uncertainty. The proposed algorithm is agnostic with respect to the dynamical model used for the refinement, provided the solution remains close enough to the initial guess. Since a computationally efficient propagator is however desirable at this stage, the analytical formulation of the J_2 -perturbed dynamics proposed in [19] is used for all numerical simulations presented in Section 4.

3 Perturbed initial orbit determination

This section describes the core of the IOD algorithms, namely the computation of a Taylor expansion of the SO's state at the IOD epoch as a function of the uncertainty on the input measurements. These computations are wrapped within the ADS algorithm introduced in Section 2.2 to control the accuracy of the final solution. If no split is triggered, the object state is represented as a single polynomial $[\mathbf{x}]$. Instead, if one or more splits are required to satisfy the threshold imposed on the truncation error, the same state is described by a manifold of polynomials $M_{\mathbf{x}}$ as defined in Eq. (8). A solution to the IOD problem is presented for the three different types of ground based sensors: range radars (Section 3.1), Doppler-only radars (Section 3.2) and optical telescopes (Section 3.3).

3.1 Range radars

Consider a range radar whose () and () are identified by the geodetic coordinates (ϕ_r, λ_r, h_r) and (ϕ_t, λ_t, h_t) , with $\phi_{r,t} \in [-\pi/2, \pi/2]$ geodetic latitude, $\lambda_{r,t} \in [-\pi, \pi]$ geodetic longitude and $h_{r,t} \in \mathbb{R}_{\geq 0}$ geodetic height of receiver and transmitter, respectively. For each detection instant, three observables are provided. The first two measurements, named azimuth ϑ and elevation φ , define the angular position of the space object (SO) in the receiver topocentric reference frame. The former provides the angular displacement of the object from the North as measured eastwards on the local horizon, such that $\vartheta \in [0, 2\pi]$. The latter is the angle between the line of sight and the horizon, $\varphi \in [-\pi/2, \pi/2]$. The third observable is instead the slant range $d = \rho_r + \rho_t$, i.e. the sum of the distances of the object from the receiver and transmitter as shown in Fig. 1.

Denote with $\mathbf{x} = [\mathbf{r}^T \mathbf{v}^T]^T$ the inertial state vector of the tracked SO and with \mathbf{r}_r the inertial position of the radar receiver at the same epoch. The relation between the two position vectors \mathbf{r} and \mathbf{r}_r can be expressed as

$$\mathbf{r} = \mathbf{r}_r + \rho \mathbf{R} \boldsymbol{\rho}_u \quad (23)$$

The unit vector $\boldsymbol{\rho}_u$ is the line of sight as expressed in the receiver topocentric frame, i.e.

$$\boldsymbol{\rho}_u = \begin{bmatrix} \cos \vartheta \cos \varphi \\ -\sin \vartheta \cos \varphi \\ \sin \varphi \end{bmatrix} \quad (24)$$

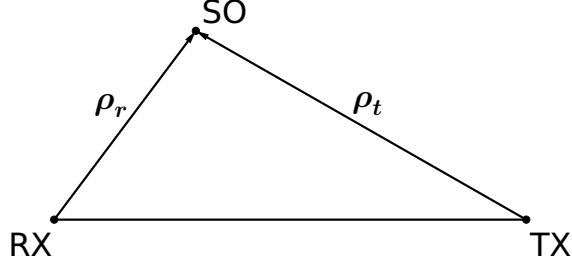


Figure 1: Geometry of bistatic radar sensor

The matrix \mathbf{R} is a time-dependent rotational matrix that converts ρ_u from the receiver topocentric to the inertial frame [20], whereas $\rho = \rho_r$ is the object range as measured from the receiver. The last is not directly available, but can be retrieved by knowing the angular position of the object, the slant range, and the location of receiver and transmitter, i.e. $\rho = \rho(\vartheta, \varphi, d, \mathbf{r}_r, \mathbf{r}_t)$ [11].

3.1.1 Initial orbit determination

Consider a set of N tuples of angular and slant range measurements as provided by a ground based range radar while observing an unknown object

$$\{t_i; (\vartheta_i; \sigma_{\vartheta_i}), (\varphi_i; \sigma_{\varphi_i}), (d_i; \sigma_{d_i})\} \quad i \in [1, N] \quad (25)$$

with $\vartheta_i, \varphi_i, d_i$ azimuth, elevation and slant range of the object at epoch t_i and $\sigma_{\alpha_i}, \sigma_{\delta_i}, \sigma_{d_i}$ the associated standard deviations of the sensor noise, assumed as uncorrelated white noise. The approach presented here extends the method proposed by [15] to perturbed orbital dynamics, providing a mathematical expression of the uncertainty on the state estimate as a function of the deviations in the nominal measurements. The first step consists in having a preliminary estimate of the full orbital state at epoch t_1 . Knowing the angular position and the slant ranges at the first and final epochs, here defined as t_1 and t_2 , the inertial positions of the object \mathbf{r}_1 and \mathbf{r}_2 are automatically known by applying geometrical considerations [11] and Eqs. (23) and (24). An estimate of the velocities at the same epochs is then obtained by solving the Lambert's problem [8] in $[t_1, t_2]$ as

$$\mathcal{L}(t_1, \mathbf{r}_1, t_2, \mathbf{r}_2) \rightarrow \{\mathbf{v}_{1,\mathcal{K}}, \mathbf{v}_{2,\mathcal{K}}\} \quad (26)$$

where the subscript \mathcal{K} indicates that the two velocities have been obtained under the hypothesis of Keplerian dynamics. Once an estimate of the orbital state at t_1 is available, a correction is computed to account for the perturbed dynamics and the uncertainty on the measurements. The angular and range measurements at t_1 and t_2 are initialized as DA variables, i.e.

$$\begin{aligned} [\vartheta_j] &= \bar{\vartheta}_j + \beta_{\vartheta_j} \delta\vartheta_j \\ [\varphi_j] &= \bar{\varphi}_j + \beta_{\varphi_j} \delta\varphi_j \\ [d_j] &= \bar{d}_j + \beta_{d_j} \delta d_j \end{aligned} \quad (27)$$

where $\bar{\vartheta}_j, \bar{\varphi}_j, \bar{d}_j$ are the nominal measurements and $\beta_{\vartheta_j}, \beta_{\varphi_j}, \beta_{d_j}$ the associated uncertainty scaling factors given by Eq. (21) or Eq. (22) for $j = 1, 2$. The Taylor expansions of the inertial positions of the object at the two epochs can be then computed as

$$[\mathbf{r}_j] = \mathcal{T}_{\mathbf{r}_j}(\delta\vartheta_j, \delta\varphi_j, \delta d_j) \quad (28)$$

By considering three additional DA variables, the expansion of the velocity at t_1 can be written as

$$[\mathbf{v}_1] = \mathbf{v}_{1,\mathcal{K}} + \delta\mathbf{v}_1 = \mathcal{T}_{\mathbf{v}_1}(\delta\mathbf{v}_1) \quad (29)$$

where $\mathbf{v}_{1,\mathcal{K}}$ is given by Eq. (26) and $\delta\mathbf{v}_1 = \{\delta v_{1,x}, \delta v_{1,y}, \delta v_{1,z}\}$. As a result, the Taylor expansion of the orbital state at epoch t_1 can be expressed as

$$[\mathbf{x}_1] = \begin{Bmatrix} [\mathbf{r}_1] \\ [\mathbf{v}_1] \end{Bmatrix} = \begin{Bmatrix} \mathcal{T}_{\mathbf{r}_1}(\delta\vartheta_1, \delta\varphi_1, \delta d_1) \\ \mathcal{T}_{\mathbf{v}_1}(\delta\mathbf{v}_1) \end{Bmatrix} = \mathcal{T}_{\mathbf{x}_1}(\delta\vartheta_1, \delta\varphi_1, \delta d_1, \delta\mathbf{v}_1) \quad (30)$$

The orbital state $[\mathbf{x}_1]$ is then propagated to t_2 under perturbed dynamics to obtain the estimated state at t_2

$$[\hat{\mathbf{x}}_2] = \begin{Bmatrix} [\hat{\mathbf{r}}_2] \\ [\hat{\mathbf{v}}_2] \end{Bmatrix} = \mathcal{T}_{\hat{\mathbf{x}}_2}(\delta\vartheta_1, \delta\varphi_1, \delta d_1, \delta\mathbf{v}_1) \quad (31)$$

The hat symbol indicates that the quantity is an estimate resulting from the perturbed propagation process, and is used from now on whenever the perturbed dynamics comes into play. At this point, the difference between the inertial position vectors at t_2 as obtained from Eqs. (28) and (31) is expressed as

$$\begin{aligned} [\Delta \hat{\mathbf{r}}_2] &= [\hat{\mathbf{r}}_2] - [\mathbf{r}_2] = \mathcal{T}_{\hat{\mathbf{r}}_2}(\delta\vartheta_1, \delta\varphi_1, \delta d_1, \delta \mathbf{v}_1) - \mathcal{T}_{\mathbf{r}_2}(\delta\vartheta_2, \delta\varphi_2, \delta d_2) \\ &= \mathcal{T}_{\Delta \hat{\mathbf{r}}_2}(\delta\boldsymbol{\vartheta}, \delta\boldsymbol{\varphi}, \delta \mathbf{d}, \delta \mathbf{v}_1) \end{aligned} \quad (32)$$

where $\delta\boldsymbol{\vartheta} = \{\delta\vartheta_1, \delta\vartheta_2\}$, $\delta\boldsymbol{\varphi} = \{\delta\varphi_1, \delta\varphi_2\}$ and $\delta \mathbf{d} = \{\delta d_1, \delta d_2\}$. Equation (32) is then split into its constant part and polynomial expansion, namely

$$[\Delta \hat{\mathbf{r}}_2] = \Delta \hat{\mathbf{r}}_2 + \mathcal{T}_{\Delta \hat{\mathbf{r}}_2}(\delta\boldsymbol{\vartheta}, \delta\boldsymbol{\varphi}, \delta \mathbf{d}, \delta \mathbf{v}_1) \quad (33)$$

an augmented map is then built as

$$\begin{Bmatrix} \delta\boldsymbol{\vartheta} \\ \delta\boldsymbol{\varphi} \\ \delta \mathbf{d} \\ \delta \hat{\mathbf{r}}_2 \end{Bmatrix} = \begin{Bmatrix} \delta\boldsymbol{\vartheta} \\ \delta\boldsymbol{\varphi} \\ \delta \mathbf{d} \\ \mathcal{T}_{\Delta \hat{\mathbf{r}}_2}(\delta\boldsymbol{\vartheta}, \delta\boldsymbol{\varphi}, \delta \mathbf{d}, \delta \mathbf{v}_1) \end{Bmatrix} \quad (34)$$

and map inversion is exploited to obtain

$$\delta \mathbf{v}_1 = \mathcal{T}_{\delta \mathbf{v}_1}(\delta\boldsymbol{\vartheta}, \delta\boldsymbol{\varphi}, \delta \mathbf{d}, \delta \hat{\mathbf{r}}_2) \quad (35)$$

The dependency of $[\mathbf{x}_1]$ on $\delta \mathbf{v}_1$ is then removed by composing Eq. (30) with Eq. (35)

$$\begin{aligned} [\hat{\mathbf{x}}_1] &= \mathcal{T}_{\mathbf{x}_1}(\delta\vartheta_1, \delta\varphi_1, \delta d_1, \delta \mathbf{v}_1) \circ \mathcal{T}_{\delta \mathbf{v}_1}(\delta\boldsymbol{\vartheta}, \delta\boldsymbol{\varphi}, \delta \mathbf{d}, \delta \hat{\mathbf{r}}_2) \\ &= \mathcal{T}_{\hat{\mathbf{x}}_1}(\delta\boldsymbol{\vartheta}, \delta\boldsymbol{\varphi}, \delta \mathbf{d}, \delta \hat{\mathbf{r}}_2) \end{aligned} \quad (36)$$

The continuity of the inertial position of the object at t_2 can be finally enforced by evaluating Eq. (36) into $(\delta\boldsymbol{\vartheta}, \delta\boldsymbol{\varphi}, \delta \mathbf{d}, -\Delta \hat{\mathbf{r}}_2)$, thus obtaining

$$\begin{aligned} [\hat{\mathbf{x}}_1] &= \mathcal{T}_{\hat{\mathbf{x}}_1}(\delta\boldsymbol{\vartheta}, \delta\boldsymbol{\varphi}, \delta \mathbf{d}, \delta \hat{\mathbf{r}}_2) \circ (\delta\boldsymbol{\vartheta}, \delta\boldsymbol{\varphi}, \delta \mathbf{d}, -\Delta \hat{\mathbf{r}}_2) \\ &= \mathcal{T}_{\hat{\mathbf{x}}_1}(\delta\boldsymbol{\vartheta}, \delta\boldsymbol{\varphi}, \delta \mathbf{d}) \end{aligned} \quad (37)$$

As a result, the Taylor expansion of the orbital state at epoch t_1 expressed in terms of the deviations from the nominal measurements is obtained.

3.2 Doppler-only radars

Consider a Doppler-only radar whose receiver and transmitter are identified by the geodetic coordinates (ϕ_r, λ_r, h_r) and (ϕ_t, λ_t, h_t) , with $\phi_{r,t} \in [-\pi/2, \pi/2]$ geodetic latitude, $\lambda_{r,t} \in [-\pi, \pi]$ geodetic longitude and $h_{r,t} \in \mathbb{R}_{\geq 0}$ geodetic height of receiver and transmitter, respectively. At each detection epoch, three observables are provided. The first two are the object azimuth and elevation as measured by the receiver (see Section 3.1). The third quantity is the range rate, defined as the time derivative \dot{d} of the slant range d introduced in Section 3.1. Now denote with $\mathbf{x} = [\mathbf{r}^T \mathbf{v}^T]^T$ the inertial state vector of the tracked SO, and with \mathbf{r}_r the inertial position of the radar receiver at the same epoch. The relation between the two position vectors \mathbf{r} and \mathbf{r}_r is still given by Eq. (23). The range ρ is however not available and shall be estimated as explained hereafter.

3.2.1 Initial orbit determination

Consider a set of N tuples of angular and range rate measurements as provided by a ground based Doppler radar while observing an unknown object

$$\left\{ t_i; (\vartheta_i; \sigma_{\vartheta_i}), (\varphi_i; \sigma_{\varphi_i}), (\dot{d}_i; \sigma_{\dot{d}_i}) \right\} \quad i \in [1, N] \quad (38)$$

with $\vartheta_i, \varphi_i, \dot{d}_i$ azimuth, elevation and range rate of the object at epoch t_i and $\sigma_{\alpha_i}, \sigma_{\delta_i}, \sigma_{\dot{d}_i}$ the associated standard deviations of the sensor noise, assumed as uncorrelated white noise. Similarly to the range radar case, DA techniques can be exploited to estimate both the nominal state and the uncertainty of the transiting object. Unlike the previous case, however, the lack of range information introduces an additional challenge that shall be faced while estimating the orbital state. The approach proposed here represents an extension of the algorithm by [16], and runs in two phases, namely range estimation and state estimate expansion.

Range estimation Consider the sets of angular measurements at the first (t_1), middle (t_2), and last (t_3) observation epochs, i.e. $(\vartheta_1; \varphi_1)$, $(\vartheta_2; \varphi_2)$, $(\vartheta_3; \varphi_3)$. A Gauss' problem can be set up, thus obtaining an estimate of the object ranges at the three epochs, i.e.

$$\mathcal{G}(t_1, \vartheta_1, \varphi_1, t_2, \vartheta_2, \varphi_2, t_3, \vartheta_3, \varphi_3) \rightarrow \{\rho_{1,\mathcal{K}}, \rho_{2,\mathcal{K}}, \rho_{3,\mathcal{K}}\} \quad (39)$$

where the subscript \mathcal{K} indicates that Keplerian dynamics is assumed. The ranges at the first and last epoch are then initialized as DA variables, namely

$$[\rho_j] = \rho_{j,\mathcal{K}} + \delta\rho_j \quad (40)$$

with $j = 1, 3$. As a result, the inertial positions at t_1 and t_3 can be built using Eqs. (23) and (24), thus obtaining

$$[\mathbf{r}_j] = \mathcal{T}_{\mathbf{r}_j}(\delta\rho_j) \quad (41)$$

An estimate for the velocity vector at t_1 is then obtained by solving the Lambert's problem in $[t_1, t_3]$ and initializing the output as a DA variable as in Eq. (29). The six-dimensional orbital state is then built as

$$[\mathbf{x}_1] = \begin{Bmatrix} [\mathbf{r}_1] \\ [\mathbf{v}_1] \end{Bmatrix} = \begin{Bmatrix} \mathcal{T}_{\mathbf{r}_1}(\delta\rho_1) \\ \mathbf{v}_{1,\mathcal{K}} + \delta\mathbf{v}_1 \end{Bmatrix} = \mathcal{T}_{\mathbf{x}_1}(\delta\rho_1, \delta\mathbf{v}_1) \quad (42)$$

Propagating $[\mathbf{x}_1]$ to t_3 under perturbed dynamics then leads to

$$[\hat{\mathbf{x}}_3] = \mathcal{T}_{\hat{\mathbf{x}}_3}(\delta\rho_1, \delta\mathbf{v}_1) \quad (43)$$

The position residuals at t_3 are then obtained from Eqs. (41) and (43)

$$\begin{aligned} [\Delta\hat{\mathbf{r}}_3] &= [\hat{\mathbf{r}}_3] - [\mathbf{r}_3] = \mathcal{T}_{\hat{\mathbf{r}}_3}(\delta\rho_1, \delta\mathbf{v}_1) - \mathcal{T}_{\mathbf{r}_3}(\delta\rho_3) \\ &= \Delta\hat{\mathbf{r}}_3 + \mathcal{T}_{\delta\hat{\mathbf{r}}_3}(\delta\rho, \delta\mathbf{v}_1) \end{aligned} \quad (44)$$

where $\delta\rho = \{\delta\rho_1, \delta\rho_3\}$. An augmented map is then built as

$$\begin{Bmatrix} \delta\rho \\ \delta\hat{\mathbf{r}}_3 \end{Bmatrix} = \begin{Bmatrix} \delta\rho \\ \mathcal{T}_{\delta\hat{\mathbf{r}}_3}(\delta\rho, \delta\mathbf{v}_1) \end{Bmatrix} \quad (45)$$

and map inversion can be exploited to obtain the Taylor expansion of $\delta\mathbf{v}_1$ as a function of $\delta\rho$ and $\delta\hat{\mathbf{r}}_3$, i.e.

$$\delta\mathbf{v}_1 = \mathcal{T}_{\delta\mathbf{v}_1}(\delta\rho, \delta\hat{\mathbf{r}}_3) \quad (46)$$

The dependency of $[\mathbf{x}_1]$ and $[\hat{\mathbf{x}}_3]$ on $\delta\mathbf{v}_1$ is then removed by composing Eqs. (42) and (43) with Eq. (46)

$$\begin{aligned} [\hat{\mathbf{x}}_1] &= \mathcal{T}_{\mathbf{x}_1}(\delta\rho_1, \delta\mathbf{v}_1) \circ \mathcal{T}_{\delta\mathbf{v}_1}(\delta\rho, \delta\hat{\mathbf{r}}_3) = \mathcal{T}_{\hat{\mathbf{x}}_1}(\delta\rho, \delta\hat{\mathbf{r}}_3) \\ [\hat{\mathbf{x}}_3] &= \mathcal{T}_{\hat{\mathbf{x}}_3}(\delta\rho_1, \delta\mathbf{v}_1) \circ \mathcal{T}_{\delta\mathbf{v}_1}(\delta\rho, \delta\hat{\mathbf{r}}_3) = \mathcal{T}_{\hat{\mathbf{x}}_3}(\delta\rho, \delta\hat{\mathbf{r}}_3) \end{aligned} \quad (47)$$

The continuity of the position vectors at t_3 is finally enforced by evaluating Eq. (47) in $(\delta\rho, -\Delta\hat{\mathbf{r}}_3)$, thus obtaining

$$\begin{aligned} [\hat{\mathbf{x}}_1] &= \mathcal{T}_{\hat{\mathbf{x}}_1}(\delta\rho, \delta\hat{\mathbf{r}}_3) \circ (\delta\rho, -\Delta\hat{\mathbf{r}}_3) = \mathcal{T}_{\hat{\mathbf{x}}_1}(\delta\rho) \\ [\hat{\mathbf{x}}_3] &= \mathcal{T}_{\hat{\mathbf{x}}_3}(\delta\rho, \delta\hat{\mathbf{r}}_3) \circ (\delta\rho, -\Delta\hat{\mathbf{r}}_3) = \mathcal{T}_{\hat{\mathbf{x}}_3}(\delta\rho) \end{aligned} \quad (48)$$

The described process removes the dependency on $\delta\mathbf{v}_1$ but does not resolve the ambiguity on the range variables, which needs to be solved for. This is solved by imposing the matching between estimated and measured range rates at t_1 and t_3 . More specifically, starting from Eq. (48), the estimate of the Taylor expansion of the range rates at the two epochs can be written as

$$\begin{bmatrix} \hat{d}_j \end{bmatrix} = \mathcal{T}_{\hat{d}_j}(\delta\rho) \quad (49)$$

for $j = 1, 3$. The difference between estimated and measured rates is then expressed as

$$\begin{aligned} [\Delta\hat{\mathbf{d}}] &= \begin{bmatrix} \hat{d}_1 \\ \hat{d}_3 \end{bmatrix} - \dot{\mathbf{d}} \\ &= \Delta\hat{\mathbf{d}} + \mathcal{T}_{\delta\hat{\mathbf{d}}}(\delta\rho) \end{aligned} \quad (50)$$

with $\begin{bmatrix} \hat{\mathbf{d}} \end{bmatrix} = \left\{ \begin{bmatrix} \hat{d}_1 \end{bmatrix}, \begin{bmatrix} \hat{d}_3 \end{bmatrix} \right\}$ built from Eq. (49) and $\dot{\mathbf{d}} = \{\dot{d}_1, \dot{d}_3\}$ measured range rates. As a result, the map $\mathcal{T}_{\delta\hat{\mathbf{d}}}(\delta\rho)$ can be inverted to obtain the dependency of $\delta\rho$ on $\delta\hat{\mathbf{d}}$, that is

$$\delta\rho = \mathcal{T}_{\delta\rho}(\delta\hat{\mathbf{d}}) \quad (51)$$

The matching between range rates is finally enforced by evaluating Eq. (51) in $-\Delta\hat{\mathbf{d}}$, that is

$$\Delta\rho = \mathcal{T}_{\delta\rho}(-\Delta\hat{\mathbf{d}}) \quad (52)$$

The quantity $\Delta\rho$ represents the correction of the constant part of Eq. (40). Once computed, the process from Eq. (40) to (52) is repeated until the correction on ρ is below a predefined threshold, i.e. $\|\Delta\rho\| < \varepsilon$.

State estimate expansion The process described in Section 3.2.1 provides an estimate of the object range at epochs t_1 and t_3 , which in turn can be used to estimate the orbital state via Eq. (48). No information on the uncertainty of the estimate is however available at this stage. A process similar to that described in Section 3.1.1 is thus set up to exploit the measurements accuracy to estimate the uncertainty on the computed solution.

Consider the available measurements at epochs t_1 and t_3 and initialize them as DA variables, i.e.

$$\begin{aligned} [\vartheta_j] &= \bar{\vartheta}_j + \beta_{\vartheta_j} \delta\vartheta_j \\ [\varphi_j] &= \bar{\varphi}_j + \beta_{\varphi_j} \delta\varphi_j \\ [\dot{d}_j] &= \bar{\dot{d}}_j + \beta_{\dot{d}_j} \delta\dot{d}_j \end{aligned} \quad (53)$$

with $\bar{\vartheta}_j, \bar{\varphi}_j, \bar{\dot{d}}_j$ the nominal measurements and $\beta_{\vartheta_j}, \beta_{\varphi_j}, \beta_{\dot{d}_j}$ the uncertainty scaling factors given by Eq. (21) or Eq. (22) for $j = 1, 3$. Similarly, the estimated ranges can be expressed as

$$[\rho_j] = \rho_j + \delta\rho_j \quad (54)$$

where the ρ_j are the results of the estimation process described in Section 3.2.1. Knowing the lines of sight and the ranges, the Taylor expansion of the inertial position vectors can be expressed as

$$[\mathbf{r}_j] = \mathcal{T}_{\mathbf{r}_j} (\delta\vartheta_j, \delta\varphi_j, \delta\rho_j) \quad (55)$$

The Taylor expansion of the orbital state at epoch t_1 is then given by

$$[\mathbf{x}_1] = \begin{Bmatrix} [\mathbf{r}_1] \\ [\mathbf{v}_1] \end{Bmatrix} = \begin{Bmatrix} \mathcal{T}_{\mathbf{r}_1} (\delta\vartheta_1, \delta\varphi_1, \delta\rho_1) \\ \mathbf{v}_1 + \delta\mathbf{v}_1 \end{Bmatrix} = \mathcal{T}_{\mathbf{x}_1} (\delta\vartheta_1, \delta\varphi_1, \delta\rho_1, \delta\mathbf{v}_1) \quad (56)$$

where \mathbf{v}_1 is available after the range estimation phase. The state is then propagated to t_3 under perturbed dynamics, thus obtaining

$$[\hat{\mathbf{x}}_3] = \mathcal{T}_{\hat{\mathbf{x}}_3} (\delta\vartheta_1, \delta\varphi_1, \delta\rho_1, \delta\mathbf{v}_1) \quad (57)$$

The position residuals at t_3 are then obtained from Eqs. (55) and (57) as

$$[\Delta\hat{\mathbf{r}}_3] = [\hat{\mathbf{r}}_3] - [\mathbf{r}_3] = \Delta\hat{\mathbf{r}}_3 + \mathcal{T}_{\delta\hat{\mathbf{r}}_3} (\delta\vartheta, \delta\varphi, \delta\rho, \delta\mathbf{v}_1) \quad (58)$$

An augmented map is then built as

$$\begin{Bmatrix} \delta\vartheta \\ \delta\varphi \\ \delta\rho \\ \delta\hat{\mathbf{r}}_3 \end{Bmatrix} = \begin{Bmatrix} \delta\vartheta \\ \delta\varphi \\ \delta\rho \\ \mathcal{T}_{\delta\hat{\mathbf{r}}_3} (\delta\vartheta, \delta\varphi, \delta\rho, \delta\mathbf{v}_1) \end{Bmatrix} \quad (59)$$

and map inversion is exploited to obtain

$$\delta\mathbf{v}_1 = \mathcal{T}_{\delta\mathbf{v}_1} (\delta\vartheta, \delta\varphi, \delta\rho, \delta\hat{\mathbf{r}}_3) \quad (60)$$

By composing Eq. (56) and (57) with Eq. (60), and then evaluating the resulting polynomials in $(\delta\vartheta, \delta\varphi, \delta\rho, -\Delta\hat{\mathbf{r}}_3)$, the following expansions are obtained

$$\begin{aligned} [\hat{\mathbf{x}}_1] &= \mathcal{T}_{\hat{\mathbf{x}}_1} (\delta\vartheta, \delta\varphi, \delta\rho) \\ [\hat{\mathbf{x}}_3] &= \mathcal{T}_{\hat{\mathbf{x}}_3} (\delta\vartheta, \delta\varphi, \delta\rho) \end{aligned} \quad (61)$$

These expansions guarantee the matching of the position vectors at t_3 but do not consider the range rate measurements at the two epochs. To enforce this matching and obtain a Taylor expansion function of the observables only, a second map inversion is exploited. More specifically, starting from Eq. (61), the estimated range rates at epoch t_1 and t_3 can be computed as

$$[\hat{\dot{d}}_j] = \mathcal{T}_{\hat{\dot{d}}_j} (\delta\vartheta, \delta\varphi, \delta\rho) \quad (62)$$

The difference between the estimated and measured range rates at the two epochs is then expressed as

$$\begin{aligned} [\Delta\hat{\dot{d}}_j] &= [\hat{\dot{d}}_j] - [\dot{d}_j] = \mathcal{T}_{\hat{\dot{d}}_j} (\delta\vartheta, \delta\varphi, \delta\rho) - \mathcal{T}_{\dot{d}_j} (\delta\dot{d}_j) \\ &= \mathcal{T}_{\Delta\hat{\dot{d}}_j} (\delta\vartheta, \delta\varphi, \delta\dot{d}_j, \delta\rho) \\ &= \Delta\hat{\dot{d}}_j + \mathcal{T}_{\delta\hat{\dot{d}}_j} (\delta\vartheta, \delta\varphi, \delta\dot{d}_j, \delta\rho) \end{aligned} \quad (63)$$

By considering the residuals at both epochs Eq. (63) is reformulated as

$$\begin{aligned} [\Delta \hat{\mathbf{d}}] &= \begin{Bmatrix} [\Delta \hat{d}_1] \\ [\Delta \hat{d}_3] \end{Bmatrix} = \begin{Bmatrix} \Delta \hat{d}_1 + \mathcal{T}_{\delta \hat{d}_1}(\delta \boldsymbol{\vartheta}, \delta \boldsymbol{\varphi}, \delta \dot{d}_1, \delta \boldsymbol{\rho}) \\ \Delta \hat{d}_3 + \mathcal{T}_{\delta \hat{d}_3}(\delta \boldsymbol{\vartheta}, \delta \boldsymbol{\varphi}, \delta \dot{d}_3, \delta \boldsymbol{\rho}) \end{Bmatrix} \\ &= \Delta \hat{\mathbf{d}} + \mathcal{T}_{\delta \hat{\mathbf{d}}}(\delta \boldsymbol{\vartheta}, \delta \boldsymbol{\varphi}, \delta \dot{\mathbf{d}}, \delta \boldsymbol{\rho}) \end{aligned} \quad (64)$$

An augmented map is then built

$$\begin{Bmatrix} \delta \boldsymbol{\vartheta} \\ \delta \boldsymbol{\varphi} \\ \delta \dot{\mathbf{d}} \\ \delta \hat{\mathbf{d}} \end{Bmatrix} = \begin{Bmatrix} \delta \boldsymbol{\vartheta} \\ \delta \boldsymbol{\varphi} \\ \delta \dot{\mathbf{d}} \\ \mathcal{T}_{\delta \hat{\mathbf{d}}}(\delta \boldsymbol{\vartheta}, \delta \boldsymbol{\varphi}, \delta \dot{\mathbf{d}}, \delta \boldsymbol{\rho}) \end{Bmatrix} \quad (65)$$

from which map inversion gives

$$\delta \boldsymbol{\rho} = \mathcal{T}_{\delta \boldsymbol{\rho}}(\delta \boldsymbol{\vartheta}, \delta \boldsymbol{\varphi}, \delta \dot{\mathbf{d}}, \delta \hat{\mathbf{d}}) \quad (66)$$

The dependency of $[\hat{\mathbf{x}}_j]$ on $\delta \boldsymbol{\rho}$ is then removed by composing Eq. (61) with Eq. (66)

$$\begin{aligned} [\hat{\mathbf{x}}_j] &= \mathcal{T}_{\hat{\mathbf{x}}_j}(\delta \boldsymbol{\vartheta}, \delta \boldsymbol{\varphi}, \delta \boldsymbol{\rho}) \circ \mathcal{T}_{\delta \boldsymbol{\rho}}(\delta \boldsymbol{\vartheta}, \delta \boldsymbol{\varphi}, \delta \dot{\mathbf{d}}, \delta \hat{\mathbf{d}}) \\ &= \mathcal{T}_{\hat{\mathbf{x}}_j}(\delta \boldsymbol{\vartheta}, \delta \boldsymbol{\varphi}, \delta \dot{\mathbf{d}}, \delta \hat{\mathbf{d}}) \end{aligned} \quad (67)$$

The matching of Doppler shift measurements at t_1 and t_3 can be finally enforced by evaluating Eq. (67) in $(\delta \boldsymbol{\vartheta}, \delta \boldsymbol{\varphi}, \delta \dot{\mathbf{d}}, -\Delta \hat{\mathbf{d}})$, thus obtaining

$$\begin{aligned} [\hat{\mathbf{x}}_j] &= \mathcal{T}_{\hat{\mathbf{x}}_j}(\delta \boldsymbol{\vartheta}, \delta \boldsymbol{\varphi}, \delta \dot{\mathbf{d}}, \delta \hat{\mathbf{d}}) \circ (\delta \boldsymbol{\vartheta}, \delta \boldsymbol{\varphi}, \delta \dot{\mathbf{d}}, -\Delta \hat{\mathbf{d}}) \\ &= \mathcal{T}_{\hat{\mathbf{x}}_j}(\delta \boldsymbol{\vartheta}, \delta \boldsymbol{\varphi}, \delta \dot{\mathbf{d}}) \end{aligned} \quad (68)$$

3.3 Optical telescopes

Consider an optical telescope identified by its geodetic coordinates (ϕ, λ, h) with $\phi \in [-\pi/2, \pi/2]$ geodetic latitude, $\lambda \in [-\pi, \pi]$ geodetic longitude and $h \in \mathbb{R}_{\geq 0}$ geodetic height. Denote with $\mathbf{x} = [\mathbf{r}^T \mathbf{v}^T]^T$ the inertial state vector of the tracked object and with \mathbf{r}_{obs} the inertial position of the telescope at the same epoch. The two positions \mathbf{r} and \mathbf{r}_{obs} are related by

$$\mathbf{r} = \mathbf{r}_{obs} + \rho \boldsymbol{\rho}_u \quad (69)$$

with ρ topocentric range and $\boldsymbol{\rho}_u$ line of sight (LOS) unit vector. The last is computed from the topocentric right ascension and declination (α, δ) as

$$\boldsymbol{\rho}_u = \begin{bmatrix} \cos \alpha \cos \delta \\ \sin \alpha \cos \delta \\ \sin \delta \end{bmatrix} \quad (70)$$

3.3.1 Initial orbit determination

Consider a set of N tuples of angular measurements as provided by a ground based optical sensor while observing an unknown SO

$$\{t_i; (\alpha_i; \sigma_{\alpha_i}), (\delta_i; \sigma_{\delta_i})\} \quad i \in [1, N] \quad (71)$$

with α_i, δ_i topocentric right ascension and declination of the SO at epoch t_i and $\sigma_{\alpha_i}, \sigma_{\delta_i}$ associated standard deviations of the sensor noise, assumed as uncorrelated white noise. The algorithm proposed here builds on [14] to provide an estimate of the orbital solution and the associated uncertainty when considering a perturbed dynamics. Similarly to the Doppler radar case, the method consists in two phases, which are described hereafter.

Range estimation Consider the sets of angular measurements at the first (t_1), middle (t_2), and last (t_3) observation epochs, i.e. $(\alpha_1; \delta_1), (\alpha_2; \delta_2), (\alpha_3; \delta_3)$. A Gauss' problem is firstly solved to obtain an estimate of the object's ranges

$$\mathcal{G}(t_1, \alpha_1, \delta_1, t_2, \alpha_2, \delta_2, t_3, \alpha_3, \delta_3) \rightarrow \{\rho_{1,\mathcal{K}}, \rho_{2,\mathcal{K}}, \rho_{3,\mathcal{K}}\} \quad (72)$$

The three ranges $[\rho_j]$ are then initialized as DA variables as in Eq. (40) and an expression for the SO's positions $[r_j]$ is computed similarly to Eq. (41). Following the procedure described in Section 3.2.1, a Taylor expansion of the orbital state at t_1 , t_2 and t_3 is then retrieved as in Eq. (42)

$$[\mathbf{x}_j] = \mathcal{T}_{\mathbf{x}_j}(\delta\rho_j, \delta\mathbf{v}_j) \quad (73)$$

where $j = 1, 2, 3$. The state vector $[\mathbf{x}_1]$ is then propagated to t_2 , thus obtaining

$$[\hat{\mathbf{x}}_2^-] = \mathcal{T}_{\hat{\mathbf{x}}_2^-}(\delta\rho_1, \delta\mathbf{v}_1) \quad (74)$$

where the minus indicates that the estimate is obtained starting from the state expansion at the earlier epoch t_1 . The Taylor expansion of the position residuals at t_2 is then written as

$$\begin{aligned} [\Delta\hat{\mathbf{r}}_2^-] &= [\hat{\mathbf{r}}_2^-] - [\mathbf{r}_2] = \mathcal{T}_{\hat{\mathbf{r}}_2^-}(\delta\rho_1, \delta\mathbf{v}_1) - \mathcal{T}_{\mathbf{r}_2}(\delta\rho_2) \\ &= \Delta\hat{\mathbf{r}}_2^- + \mathcal{T}_{\delta\hat{\mathbf{r}}_2^-}(\delta\rho_{12}, \delta\mathbf{v}_1) \end{aligned} \quad (75)$$

where $\delta\rho_{12} = \{\delta\rho_1, \delta\rho_2\}$. An augmented map is then built

$$\begin{Bmatrix} \delta\rho_{12} \\ \delta\hat{\mathbf{r}}_2^- \end{Bmatrix} = \begin{Bmatrix} \delta\rho_{12} \\ \mathcal{T}_{\delta\hat{\mathbf{r}}_2^-}(\delta\rho_{12}, \delta\mathbf{v}_1) \end{Bmatrix} \quad (76)$$

and map inversion is exploited to obtain the Taylor expansion of $\delta\mathbf{v}_1$, i.e.

$$\delta\mathbf{v}_1 = \mathcal{T}_{\delta\mathbf{v}_1}(\delta\rho_{12}, \delta\hat{\mathbf{r}}_2^-) \quad (77)$$

Composing this expression with the Taylor expansion of the orbital states at t_1 and t_2 gives

$$\begin{aligned} [\hat{\mathbf{x}}_1] &= \mathcal{T}_{\mathbf{x}_1}(\delta\rho_1, \delta\mathbf{v}_1) \circ \mathcal{T}_{\delta\mathbf{v}_1}(\delta\rho_{12}, \delta\hat{\mathbf{r}}_2^-) = \mathcal{T}_{\hat{\mathbf{x}}_1}(\delta\rho_{12}, \delta\hat{\mathbf{r}}_2^-) \\ [\hat{\mathbf{x}}_2^-] &= \mathcal{T}_{\hat{\mathbf{x}}_2^-}(\delta\rho_1, \delta\mathbf{v}_1) \circ \mathcal{T}_{\delta\mathbf{v}_1}(\delta\rho_{12}, \delta\hat{\mathbf{r}}_2^-) = \mathcal{T}_{\hat{\mathbf{x}}_2^-}(\delta\rho_{12}, \delta\hat{\mathbf{r}}_2^-) \end{aligned} \quad (78)$$

The continuity of the position vectors at t_2 is then granted by evaluating Eq. (78) in $(\delta\rho_{12}, -\Delta\hat{\mathbf{r}}_2^-)$, thus obtaining

$$\begin{aligned} [\hat{\mathbf{x}}_1] &= \mathcal{T}_{\hat{\mathbf{x}}_1}(\delta\rho_{12}, \delta\hat{\mathbf{r}}_2^-) \circ (\delta\rho_{12}, -\Delta\hat{\mathbf{r}}_2^-) = \mathcal{T}_{\hat{\mathbf{x}}_1}(\delta\rho_{12}) \\ [\hat{\mathbf{x}}_2^-] &= \mathcal{T}_{\hat{\mathbf{x}}_2^-}(\delta\rho_{12}, \delta\hat{\mathbf{r}}_2^-) \circ (\delta\rho_{12}, -\Delta\hat{\mathbf{r}}_2^-) = \mathcal{T}_{\hat{\mathbf{x}}_2^-}(\delta\rho_{12}) \end{aligned} \quad (79)$$

The described procedure is then repeated starting from the state vector at t_3 and propagating backward to obtain $[\hat{\mathbf{x}}_2^+]$. After inverting the residuals map and imposing the continuity in position as in Eqs. (75) to (79), the following expressions are available

$$\begin{aligned} [\hat{\mathbf{x}}_2^-] &= \mathcal{T}_{\hat{\mathbf{x}}_2^-}(\delta\rho_{12}) \\ [\hat{\mathbf{x}}_2^+] &= \mathcal{T}_{\hat{\mathbf{x}}_2^+}(\delta\rho_{23}) \end{aligned} \quad (80)$$

where $\delta\rho_{23} = \{\delta\rho_2, \delta\rho_3\}$. At this point, the state vector at the middle epoch is continuous in position but not in velocity. The last is enforced by firstly computing the residuals from Eq. (80) as

$$\begin{aligned} [\Delta\hat{\mathbf{v}}_2] &= [\hat{\mathbf{v}}_2^+] - [\hat{\mathbf{v}}_2^-] = \mathcal{T}_{\hat{\mathbf{v}}_2^+}(\delta\rho_{23}) - \mathcal{T}_{\hat{\mathbf{v}}_2^-}(\delta\rho_{12}) \\ &= \mathcal{T}_{\Delta\hat{\mathbf{v}}_2}(\delta\rho) \\ &= \Delta\hat{\mathbf{v}}_2 + \mathcal{T}_{\delta\hat{\mathbf{v}}_2}(\delta\rho) \end{aligned} \quad (81)$$

where $\delta\rho = \{\rho_1, \rho_2, \rho_3\}$. The Taylor expansion $\mathcal{T}_{\delta\hat{\mathbf{v}}_2}(\delta\rho)$ is then inverted to obtain an expression of $\delta\rho$ as a function of $\delta\hat{\mathbf{v}}_2$, that is

$$\delta\rho = \mathcal{T}_{\delta\rho}(\delta\hat{\mathbf{v}}_2) \quad (82)$$

The continuity of the velocity vector at t_2 is finally enforced by evaluating Eq. (82) in $-\Delta\hat{\mathbf{v}}_2$ to obtain the required ranges updates

$$\Delta\rho = \mathcal{T}_{\delta\rho}(-\Delta\hat{\mathbf{v}}_2) \quad (83)$$

This correction is then plugged into the initialization of the ρ_j variables, and the whole process is iterated until the correction is below a predefined threshold, i.e. $\|\Delta\rho\| < \varepsilon$.

State estimate expansion Once a solution for the nominal state is obtained, DA can be exploited to estimate the associated uncertainty due to sensor noise.

Consider the available measurements at epochs t_1 , t_2 and t_3 and initialize them as DA variables, i.e.

$$\begin{aligned} [\alpha_j] &= \bar{\alpha}_j + \beta_{\alpha_j} \delta\alpha_j \\ [\delta_j] &= \bar{\delta}_j + \beta_{\delta_j} \delta\delta_j \end{aligned} \quad (84)$$

where $\bar{\alpha}_j, \bar{\delta}_j$ are the nominal measurements and $\beta_{\alpha_j}, \beta_{\delta_j}$ the uncertainty scaling factors given by Eq. (21) or Eq. (22) for $j = 1, 2, 3$. Similarly, the estimated ranges are expressed as

$$[\rho_j] = \rho_j + \delta\rho_j \quad (85)$$

where ρ_j are the results of the estimation process described in Section 3.3.1. Knowing the lines of sight and the ranges, the Taylor expansions of the inertial position vectors are computed as

$$[\mathbf{r}_j] = \mathcal{T}_{\mathbf{r}_j} (\delta\alpha_j, \delta\delta_j, \delta\rho_j) \quad (86)$$

The orbital state at epoch t_1 is then given by

$$[\mathbf{x}_1] = \begin{Bmatrix} [\mathbf{r}_1] \\ [\mathbf{v}_1] \end{Bmatrix} = \begin{Bmatrix} \mathcal{T}_{\mathbf{r}_1} (\delta\alpha_1, \delta\delta_1, \delta\rho_1) \\ \mathbf{v}_1 + \delta\mathbf{v}_1 \end{Bmatrix} = \mathcal{T}_{\mathbf{x}_1} (\delta\alpha_1, \delta\delta_1, \delta\rho_1, \delta\mathbf{v}_1) \quad (87)$$

where \mathbf{v}_1 is available from the range estimation phase. The state is then propagated to t_2 under the perturbed orbital dynamics, thus obtaining

$$[\hat{\mathbf{x}}_2^-] = \mathcal{T}_{\hat{\mathbf{x}}_2^-} (\delta\alpha_1, \delta\delta_1, \delta\rho_1, \delta\mathbf{v}_1) \quad (88)$$

The position residuals at t_2 are then computed from Eqs. (86) and (88) as

$$[\Delta\hat{\mathbf{r}}_2] = [\hat{\mathbf{r}}_2^-] - [\mathbf{r}_2] = \Delta\hat{\mathbf{r}}_2^- + \mathcal{T}_{\delta\hat{\mathbf{r}}_2^-} (\delta\alpha_{12}, \delta\delta_{12}, \delta\rho_{12}, \delta\mathbf{v}_1) \quad (89)$$

where $\delta\alpha_{12} = \{\delta\alpha_1, \delta\alpha_2\}$, $\delta\delta_{12} = \{\delta\delta_1, \delta\delta_2\}$. An augmented map is then built as

$$\begin{Bmatrix} \delta\alpha_{12} \\ \delta\delta_{12} \\ \delta\rho_{12} \\ \delta\hat{\mathbf{r}}_2^- \end{Bmatrix} = \begin{Bmatrix} \delta\alpha_{12} \\ \delta\delta_{12} \\ \delta\rho_{12} \\ \mathcal{T}_{\delta\hat{\mathbf{r}}_2^-} (\delta\alpha_{12}, \delta\delta_{12}, \delta\rho_{12}, \delta\mathbf{v}_1) \end{Bmatrix} \quad (90)$$

and map inversion is exploited to obtain

$$\delta\mathbf{v}_1 = \mathcal{T}_{\delta\mathbf{v}_1} (\delta\alpha_{12}, \delta\delta_{12}, \delta\rho_{12}, \delta\hat{\mathbf{r}}_2^-) \quad (91)$$

By composing Eq. (87) and (88) with Eq. (91), and then evaluating the resulting polynomials in $(\delta\alpha_{12}, \delta\delta_{12}, \delta\rho_{12}, -\Delta\hat{\mathbf{r}}_2^-)$, the following polynomial expansions are obtained

$$\begin{aligned} [\hat{\mathbf{x}}_1] &= \mathcal{T}_{\hat{\mathbf{x}}_1} (\delta\alpha_{12}, \delta\delta_{12}, \delta\rho_{12}) \\ [\hat{\mathbf{x}}_2^-] &= \mathcal{T}_{\hat{\mathbf{x}}_2^-} (\delta\alpha_{12}, \delta\delta_{12}, \delta\rho_{12}) \end{aligned} \quad (92)$$

The same procedure is then repeated starting from the orbital state at t_3 , thus obtaining

$$\begin{aligned} [\hat{\mathbf{x}}_2^+] &= \mathcal{T}_{\hat{\mathbf{x}}_2^+} (\delta\alpha_{23}, \delta\delta_{23}, \delta\rho_{23}) \\ [\hat{\mathbf{x}}_3] &= \mathcal{T}_{\hat{\mathbf{x}}_3} (\delta\alpha_{23}, \delta\delta_{23}, \delta\rho_{23}) \end{aligned} \quad (93)$$

where $\delta\alpha_{23} = \{\delta\alpha_2, \delta\alpha_3\}$, $\delta\delta_{23} = \{\delta\delta_2, \delta\delta_3\}$, and $\delta\rho_{23} = \{\delta\rho_2, \delta\rho_3\}$. At this point, starting from the Taylor expansions $[\hat{\mathbf{x}}_2^+]$ and $[\hat{\mathbf{x}}_2^-]$, the velocity residuals are expressed as

$$\begin{aligned} [\Delta\hat{\mathbf{v}}_2] &= [\hat{\mathbf{v}}_2^+] - [\hat{\mathbf{v}}_2^-] = \mathcal{T}_{\hat{\mathbf{v}}_2^+} (\delta\alpha_{23}, \delta\delta_{23}, \delta\rho_{23}) - \mathcal{T}_{\hat{\mathbf{v}}_2^-} (\delta\alpha_{12}, \delta\delta_{12}, \delta\rho_{12}) \\ &= \mathcal{T}_{\Delta\hat{\mathbf{v}}_2} (\delta\alpha, \delta\delta, \delta\rho) \\ &= \Delta\hat{\mathbf{v}}_2 + \mathcal{T}_{\delta\hat{\mathbf{v}}_2} (\delta\alpha, \delta\delta, \delta\rho) \end{aligned} \quad (94)$$

An augmented map is then built as

$$\begin{Bmatrix} \delta\alpha \\ \delta\delta \\ \delta\hat{\mathbf{v}}_2 \end{Bmatrix} = \begin{Bmatrix} \delta\alpha \\ \delta\delta \\ \mathcal{T}_{\delta\hat{\mathbf{v}}_2} (\delta\alpha, \delta\delta, \delta\rho) \end{Bmatrix} \quad (95)$$

and map inversion is exploited to obtain

$$\delta \boldsymbol{\rho} = \mathcal{T}_{\delta \boldsymbol{\rho}} (\delta \boldsymbol{\alpha}, \delta \boldsymbol{\delta}, \delta \hat{\boldsymbol{v}}_2) \quad (96)$$

The dependency of $[\hat{\boldsymbol{x}}_1]$ on $\delta \boldsymbol{\rho}_{12}$ is then removed by composing Eq. (92) with Eq. (96)

$$\begin{aligned} [\hat{\boldsymbol{x}}_1] &= \mathcal{T}_{\hat{\boldsymbol{x}}_1} (\delta \boldsymbol{\alpha}_{12}, \delta \boldsymbol{\delta}_{12}, \delta \boldsymbol{\rho}_{12}) \circ \mathcal{T}_{\delta \boldsymbol{\rho}} (\delta \boldsymbol{\alpha}, \delta \boldsymbol{\delta}, \delta \hat{\boldsymbol{v}}_2) \\ &= \mathcal{T}_{\hat{\boldsymbol{x}}_1} (\delta \boldsymbol{\alpha}, \delta \boldsymbol{\delta}, \delta \hat{\boldsymbol{v}}_2) \end{aligned} \quad (97)$$

Evaluating Eq. (97) in $(\delta \boldsymbol{\alpha}, \delta \boldsymbol{\delta}, -\Delta \hat{\boldsymbol{v}}_2)$ finally yields to

$$[\hat{\boldsymbol{x}}_1] = \mathcal{T}_{\hat{\boldsymbol{x}}_1} (\delta \boldsymbol{\alpha}, \delta \boldsymbol{\delta}, \delta \hat{\boldsymbol{v}}_2) \circ (\delta \boldsymbol{\alpha}, \delta \boldsymbol{\delta}, -\Delta \hat{\boldsymbol{v}}_2) = \mathcal{T}_{\hat{\boldsymbol{x}}_1} (\delta \boldsymbol{\alpha}, \delta \boldsymbol{\delta}) \quad (98)$$

which is the Taylor expansion of the orbital solution with respect to uncertainties in the available measurements.

4 Numerical simulations

This section illustrates the performance of the proposed methods obtained by means of numerical simulations. For all simulations, an expansion order of 4 was used. To control the ADS algorithm, the tolerances on the components of the state vector (the output of the function wrapped by the ADS) were set equal to 10 m and 1 mm s^{-1} in position and velocity respectively. However, no splits were observed in the analyzed scenarios. A discussion on the performance of the ADS algorithm in the context of IOD is provided in [14] for optical measurements under the assumption of Keplerian dynamics. The conclusions presented in that paper are deemed to be representative of the solution that would be obtained with the same input measurements by considering J_2 -perturbed dynamics. All the simulations were run on an Intel i7-8565U CPU @ 1.80GHz and 16GB of RAM. The algorithms were implemented in Java and interface with the CNES library PACE (Polynomial Algebra Computational Engine) to perform all DA operations.

Following the scheme described in [16], the simulations were done by considering a subset of the NORAD Low Earth Orbit (LEO) population. The analyses were carried out by downloading the latest Two Line Elements (TLE), considering a one-day propagation window in high-fidelity dynamics (including the Earth gravitational potential up to order and degree 8, the third body effect of Sun and Moon, the atmospheric drag and the solar radiation pressure), and then generating the measurements produced by different observers. In the presented analysis, two observers are considered, i.e. a Doppler-only radar and an optical telescope. The Doppler-only radar has a bistatic configuration, where the receiver has latitude $44^\circ 4' 17''$ North, longitude $5^\circ 32' 4''$ East and altitude 180 m, while the transmitter has latitude $47^\circ 20' 53''$ North, longitude $5^\circ 30' 54''$ East and altitude 180 m. The transmission site is assumed to be capable of covering the azimuth band from 90 deg to 270 deg and the elevation band from 20 deg to 40 deg, simultaneously, whereas the field of view of the receiver is assumed infinite, i.e. an object is observed whenever detected by the transmitter. The optical sensor is instead co-located with the radar transmitter. In order to increase the number of optical detection, no specific pointing direction or field of view are selected, i.e. the optical sensor is assumed to be capable of covering all the passages detected by the radar. This scenario is obviously unrealistic, but allows us to investigate a wider selection of cases. Overall, about 2,000 passages are generated. For each passage, 10 different measurement noise levels are considered. These noise levels are indicated with the symbols k_i^σ , with $i = 1, \dots, 10$. For the Doppler radar, they range from $k_1^\sigma = (0.01 \text{ deg}; 0.01 \text{ deg}; 0.1 \text{ m/s})$ to $k_{10}^\sigma = 10k_1^\sigma$, with a step $\Delta k^\sigma = k_{i+1}^\sigma - k_i^\sigma = k_1^\sigma$, with $i = 1, \dots, 9$, where each triplet indicates the noise standard deviations in azimuth, elevation, and range rate, respectively. For the optical telescope, $k_1^\sigma = (0.1 \text{ arcsec}; 0.1 \text{ arcsec})$ while $k_{10}^\sigma = 10k_1^\sigma$, with $\Delta k^\sigma = k_1^\sigma$, where each couple indicates the noise standard deviations in right ascension and declination. Overall, 20,000 passages are generated. For each passage, the proposed methods are then run by considering two different orbital dynamics: Keplerian and J_2 -perturbed dynamics [19]. The aim is to investigate how the performance of the proposed methods varies as function of the selected dynamics, arc length and noise level. Two indices are considered: ε_x and f_x . The first index is the non-dimensional error between the estimated state and the true one defined as

$$\varepsilon_x = \left\| \frac{\hat{\boldsymbol{x}} - \boldsymbol{x}}{\boldsymbol{\gamma}} \right\|_2 \quad (99)$$

where $\hat{\boldsymbol{x}}$ is the computed estimate, \boldsymbol{x} the true state and $\boldsymbol{\gamma}$ a six-dimensional vector of scaling coefficients used to normalize the error vector components. In this work, $\boldsymbol{\gamma} = \{R_E, R_E, R_E, v_c, v_c, v_c\}^T$ with R_E the equatorial radius of the Earth, $v_c = \sqrt{\mu/R_E}$ the orbital velocity on a circular orbit at R_E , and μ the Earth standard gravitational parameter. Vector subtraction and division in Eq. (99) are performed element-wise such that the argument of $\|\cdot\|_2$ is a non-dimensional error vector whose Euclidean norm is defined to be ε_x . The second index f_x is the fraction of the estimated bounds that correctly include the true state, and is computed as follows. Given the polynomial expansion of the IOD solution $[\hat{\boldsymbol{x}}]$, DA routines are used to estimate the lower and upper bounds \boldsymbol{x}^{lb} , \boldsymbol{x}^{ub} within which the former expansion satisfies the accuracy imposed by the ADS algorithm. As such, any state $\tilde{\boldsymbol{x}}$ that falls within these bounds, i.e.

$\tilde{\mathbf{x}}_i \in [\mathbf{x}_i^{lb}, \mathbf{x}_i^{ub}] \forall i \in [1, 6]$, can be accurately mapped to the deviation $\delta\tilde{\mathbf{y}}$ with respect to the nominal measurement vector \mathbf{y} that corresponds to the displaced state $\tilde{\mathbf{x}}$. Since the truncation error within these bounds is controlled by the ADS algorithm, it is of interest to quantify the ratio between the number of tuples $[\mathbf{x}_i^{lb}, \mathbf{x}_i^{ub}]$ that include the true solution \mathbf{x}_i and the total number of state components, with the last equal to the dimension of $\tilde{\mathbf{x}}$. For each component of the state a check is thus performed, and a vector of binary values is built by assigning “1” to the components for which the true state falls within the estimated bounds and “0” to the ones for which the true state lies outside. The index $f_{\mathbf{x}}$ is then taken as the arithmetic mean of these values such that $f_{\mathbf{x}} \in [0, 1]$.

		$\Delta t_{obs} < 0.03T$	$\Delta t_{obs} < 0.06T$	$\Delta t_{obs} < 0.09T$	$\Delta t_{obs} < 0.12T$
$\varepsilon_{\mathbf{x}}$ (-)	k_2^σ	9.5737×10^{-4}	6.9346×10^{-4}	6.8481×10^{-4}	6.8381×10^{-4}
	k_4^σ	1.7753×10^{-3}	1.1503×10^{-3}	1.1219×10^{-3}	1.1175×10^{-3}
	k_6^σ	2.2476×10^{-3}	1.4173×10^{-3}	1.3774×10^{-3}	1.3711×10^{-3}
	k_8^σ	2.9637×10^{-3}	1.8205×10^{-3}	1.7630×10^{-3}	1.7539×10^{-3}
	k_{10}^σ	3.8940×10^{-3}	2.3385×10^{-3}	2.2589×10^{-3}	2.2459×10^{-3}

Table 1: State errors under Keplerian dynamics (optical sensor, raw data).

		$\Delta t_{obs} < 0.03T$	$\Delta t_{obs} < 0.06T$	$\Delta t_{obs} < 0.09T$	$\Delta t_{obs} < 0.12T$
$\varepsilon_{\mathbf{x}}$ (-)	k_2^σ	9.5144×10^{-4}	5.8405×10^{-4}	5.6625×10^{-4}	5.6330×10^{-4}
	k_4^σ	1.8016×10^{-3}	1.0626×10^{-3}	1.0241×10^{-3}	1.0177×10^{-3}
	k_6^σ	2.2057×10^{-3}	1.2992×10^{-3}	1.2507×10^{-3}	1.2426×10^{-3}
	k_8^σ	2.9387×10^{-3}	1.7163×10^{-3}	1.6499×10^{-3}	1.6388×10^{-3}
	k_{10}^σ	3.8860×10^{-3}	2.2529×10^{-3}	2.1631×10^{-3}	2.1481×10^{-3}

 Table 2: State errors under J_2 dynamics (optical sensor, raw data).

Table 1 shows the performance of the proposed method in terms of $\varepsilon_{\mathbf{x}}$ when considering Keplerian dynamics on raw data collected by the optical sensor. For the sake of conciseness, only five noise levels corresponding to k_{2j}^σ , for $j = 1, \dots, 5$ are reported in all subsequent tables. The results are in fact consistent across different values of k_i^σ and no additional conclusions can thus be drawn by looking at the omitted results. All passages are sorted according to their noise level k_i^σ and the observed arc length, expressed in terms of fractions of orbital period Δt_{obs} . For all the passages falling into a specific $(k_i^\sigma; \Delta t_{obs})$ slot, the $\varepsilon_{\mathbf{x}}$ index is computed. The values reported in the table are the average per slot. Let us first analyze the trend of the error as a function of the noise level. As expected, the error of the estimate increases as the measurement accuracy decreases. Conversely, for a fixed noise level and increasing arc duration, the error progressively decreases. Given the relatively short duration of the passages (LEO objects observed during a single pass), this trend is also expected, as measurements spread on a longer arc allow the solver to better capture the curvature of the underlying orbit. Table 2 shows instead the results obtained for the same test cases when the J_2 -perturbed dynamics is considered. If on one side the trends remain the same, comparing Tables 1 and 2 slot by slot shows that the introduction of the J_2 perturbation systematically improves the accuracy of the obtained solution.

		$\Delta t_{obs} < 0.03T$	$\Delta t_{obs} < 0.06T$	$\Delta t_{obs} < 0.09T$	$\Delta t_{obs} < 0.12T$
$f_{\mathbf{x}}$ (-)	k_2^σ	0.93692	0.71859	0.68914	0.68438
	k_4^σ	0.98631	0.84882	0.81768	0.81236
	k_6^σ	0.99555	0.91394	0.88603	0.88070
	k_8^σ	0.99825	0.94397	0.92380	0.91868
	k_{10}^σ	0.99920	0.96332	0.94678	0.94199

Table 3: Bound success under Keplerian dynamics assumption (optical sensor, raw data).

The advantages granted by a more refined dynamics can be instead easily noticed investigating the accuracy of the estimated bounds. Table 3 shows the trend of the average $f_{\mathbf{x}}$ parameter as a function of noise level and arc length. Let first set the noise level at k_2^σ and consider increasingly longer arc lengths. As can be seen, the percentage of success progressively drops, passing from 93.69% to 68.44%. That is, the longer the arc, the less accurate the estimated bounds. This trend is exactly the opposite of the trend identified for $\varepsilon_{\mathbf{x}}$, for which an increase in the observed arc length was beneficial. The explanation is that as the passage duration increases, the solution becomes more and more accurate, but the estimated bounds excessively shrink around the nominal solution up to a point that they often no longer include the real state. This undesired behavior can be explained considering all the actors coming into play, i.e. noise level, arc length, and dynamics. As the arc length increases, the Keplerian assumption is less accurate. Though longer arcs allow

		$\Delta t_{obs} < 0.03T$	$\Delta t_{obs} < 0.06T$	$\Delta t_{obs} < 0.09T$	$\Delta t_{obs} < 0.12T$
f_x (-)	k_2^σ	0.98697	0.88552	0.86759	0.86500
	k_4^σ	0.99682	0.94183	0.92769	0.92565
	k_6^σ	0.99857	0.96383	0.95295	0.95088
	k_8^σ	0.99936	0.97450	0.96599	0.96390
	k_{10}^σ	0.99968	0.98263	0.97478	0.97263

 Table 4: Bound success under J_2 dynamics assumption (optical sensor, raw data).

us to better estimate the orbit, the improvements are not enough to keep up with the shrinking of the estimated bounds, which are therefore unreliable. The situation becomes less and less critical as the noise levels increase. In this case the bounds are in fact inflated by the larger uncertainty in the measurements, thus the mismatch in dynamics has almost no impact on their accuracy. Evidence of this can be noticed looking at the line for k_{10}^σ , with ε_x passing from 99.92% to 94.20%. The introduction of a higher fidelity dynamics partly mitigates this trends, thus providing a more accurate solution as the considered arc length increases, as shown in Table 4. In this case the advantage of considering the J_2 perturbation progressively increase for longer passages, with an average success rate always above 86%.

		$\Delta t_{obs} < 0.03T$	$\Delta t_{obs} < 0.06T$	$\Delta t_{obs} < 0.09T$	$\Delta t_{obs} < 0.12T$
ε_x (-)	k_2^σ	8.6631×10^{-4}	6.4234×10^{-4}	6.3596×10^{-4}	6.3532×10^{-4}
	k_4^σ	1.3874×10^{-3}	9.3380×10^{-4}	9.1481×10^{-4}	9.1209×10^{-4}
	k_6^σ	1.7112×10^{-3}	1.1187×10^{-3}	1.0917×10^{-3}	1.0876×10^{-3}
	k_8^σ	2.2265×10^{-3}	1.4056×10^{-3}	1.3660×10^{-3}	1.3599×10^{-3}
	k_{10}^σ	2.7562×10^{-3}	1.7006×10^{-3}	1.6486×10^{-3}	1.6403×10^{-3}

Table 5: State errors under Keplerian dynamics assumption (optical, regressed data).

		$\Delta t_{obs} < 0.03T$	$\Delta t_{obs} < 0.06T$	$\Delta t_{obs} < 0.09T$	$\Delta t_{obs} < 0.12T$
ε_x (-)	k_2^σ	8.2385×10^{-4}	5.1053×10^{-4}	4.9594×10^{-4}	4.9352×10^{-4}
	k_4^σ	1.3578×10^{-3}	8.0978×10^{-4}	7.8219×10^{-4}	7.7763×10^{-4}
	k_6^σ	1.6524×10^{-3}	9.7980×10^{-4}	9.4493×10^{-4}	9.3915×10^{-4}
	k_8^σ	2.2055×10^{-3}	1.2930×10^{-3}	1.2446×10^{-3}	1.2366×10^{-3}
	k_{10}^σ	2.7480×10^{-3}	1.5951×10^{-3}	1.5332×10^{-3}	1.5229×10^{-3}

 Table 6: State errors under J_2 dynamics assumption (optical, regressed data)

		$\Delta t_{obs} < 0.03T$	$\Delta t_{obs} < 0.06T$	$\Delta t_{obs} < 0.09T$	$\Delta t_{obs} < 0.12T$
f_x (-)	k_2^σ	0.83270	0.57288	0.54898	0.54494
	k_4^σ	0.93730	0.71578	0.68625	0.68135
	k_6^σ	0.97172	0.78777	0.75627	0.75100
	k_8^σ	0.98646	0.84363	0.81144	0.80600
	k_{10}^σ	0.98667	0.87489	0.84297	0.83745

Table 7: Bound success under Keplerian dynamics assumption (optical, regressed data).

		$\Delta t_{obs} < 0.03T$	$\Delta t_{obs} < 0.06T$	$\Delta t_{obs} < 0.09T$	$\Delta t_{obs} < 0.12T$
f_x (-)	k_2^σ	0.96591	0.80787	0.78814	0.78373
	k_4^σ	0.98762	0.88719	0.86905	0.86595
	k_6^σ	0.99364	0.92155	0.90493	0.90197
	k_8^σ	0.99618	0.94075	0.92505	0.92252
	k_{10}^σ	0.99631	0.95296	0.93895	0.93664

 Table 8: Bound success under J_2 dynamics assumption (optical, regressed data).

Tables 5 to 8 show the trends for the ε_x and f_x indices considering both Keplerian and J_2 perturbed dynamics when processing regressed measurements. The trends closely resemble the ones found with raw data. The introduction of

measurement regression, however, has two major effects. The first is a general improvement in the solution accuracy ε_x , as can be seen by comparing Table 5 with Table 1 and Table 6 with Table 2. Measurement regression allows in fact the solver to mitigate the effect of measurement noise, thus preventing the algorithm from underperforming due to possible local strong realizations of the measurement noise in the three observation epochs exploited for IOD. The second trend is instead a general worsening of the bounds accuracy regardless of the noise level and arc length. This behavior is also expected, as regression tends to shrink the uncertainty region around the fitted measurements. This has the undesired effect of exacerbating the impact of the orbital dynamics mismatch, and it is only partially mitigated by the introduction of the J_2 perturbations.

		$\Delta t_{obs} < 0.03T$	$\Delta t_{obs} < 0.06T$	$\Delta t_{obs} < 0.09T$	$\Delta t_{obs} < 0.12T$
ε_x (-)	k_2^σ	3.0774×10^{-3}	2.0679×10^{-3}	2.0047×10^{-3}	1.9947×10^{-3}
	k_4^σ	6.1968×10^{-3}	4.0612×10^{-3}	3.9367×10^{-3}	3.9145×10^{-3}
	k_6^σ	8.0059×10^{-3}	5.3869×10^{-3}	5.2270×10^{-3}	5.2015×10^{-3}
	k_8^σ	1.1842×10^{-2}	7.7992×10^{-3}	7.5570×10^{-3}	7.5172×10^{-3}
	k_{10}^σ	1.2601×10^{-2}	8.4968×10^{-3}	8.2419×10^{-3}	8.2036×10^{-3}

Table 9: State errors under Keplerian dynamics assumption (Doppler radar, raw data).

		$\Delta t_{obs} < 0.03T$	$\Delta t_{obs} < 0.06T$	$\Delta t_{obs} < 0.09T$	$\Delta t_{obs} < 0.12T$
ε_x (-)	k_2^σ	2.2861×10^{-3}	1.6191×10^{-3}	1.5736×10^{-3}	1.5662×10^{-3}
	k_4^σ	4.4077×10^{-3}	3.0636×10^{-3}	2.9812×10^{-3}	2.9661×10^{-3}
	k_6^σ	6.3448×10^{-3}	4.4627×10^{-3}	4.3427×10^{-3}	4.3239×10^{-3}
	k_8^σ	8.5575×10^{-3}	6.0009×10^{-3}	5.8362×10^{-3}	5.8093×10^{-3}
	k_{10}^σ	1.0053×10^{-2}	7.1072×10^{-3}	6.9136×10^{-3}	6.8856×10^{-3}

Table 10: State errors under J_2 dynamics assumption (Doppler radar, raw data)

		$\Delta t_{obs} < 0.03T$	$\Delta t_{obs} < 0.06T$	$\Delta t_{obs} < 0.09T$	$\Delta t_{obs} < 0.12T$
f_x (-)	k_2^σ	0.99839	0.99902	0.99907	0.99907
	k_4^σ	0.99742	0.99857	0.99864	0.99865
	k_6^σ	0.99804	0.99874	0.99871	0.99872
	k_8^σ	0.99583	0.99763	0.99774	0.99775
	k_{10}^σ	0.99629	0.99770	0.99780	0.99782

Table 11: Bound success under Keplerian dynamics assumption (Doppler radar, raw data).

		$\Delta t_{obs} < 0.03T$	$\Delta t_{obs} < 0.06T$	$\Delta t_{obs} < 0.09T$	$\Delta t_{obs} < 0.12T$
f_x (-)	k_2^σ	0.99952	0.99964	0.99966	0.99966
	k_4^σ	0.99936	0.99964	0.99966	0.99966
	k_6^σ	1.0000	0.99982	0.99974	0.99974
	k_8^σ	0.99983	0.99982	0.99983	0.99983
	k_{10}^σ	0.99933	0.99936	0.99938	0.99939

Table 12: Bound success under J_2 dynamics assumption (Doppler radar, raw data).

Tables 9 to 12 show the results of the application of the proposed method to raw measurements provided by the described Doppler-only bistatic radar. Tables 9 and 10 show the trend of the solution accuracy ε_x as a function of noise level and arc length. The same considerations made for optical measurements hold. Differences with respect to the optical case can instead be noticed when analyzing the trend of the f_x parameter. As can be seen, the bounds accuracy is always very high, above 99%, regardless of the noise level, arc length, or considered dynamics. This trend can be explained by considering the accuracy of the angular measurements provided by the radar. If compared with that of optical measurements, there are in fact almost three orders of magnitude of difference between them. As a result, mismatches in the dynamical model are absorbed by the large bounds estimates that result from large measurement errors, thus ensuring the true state is almost always included in the provided bounds.

5 Conclusions

This work introduced three novel initial orbit determination (IOD) algorithms for optical, range radar and Doppler-only radars. The methods combine differential algebra (DA) and automatic domain splitting (ADS) to obtain the Taylor expansion of the orbital solution as a function of uncertainties in the processed measurements. The algorithms build on previous work presented by the authors based on Keplerian dynamics and extend it to arbitrary dynamical models, thus relaxing any applicability constraint connected with observed arc length and orbital regime. The methods were tested on simulated data obtained by targeting a subset of the NORAD Low Earth Orbit (LEO) population considering an analytical formulation of the J_2 -perturbed dynamics. The comparison with their Keplerian counterpart show that the proposed approaches provide more accurate results in terms of both nominal solution and size of the estimated bounds. Future developments include testing the proposed algorithms with other dynamical models and their application to different orbital regimes.

Acknowledgements

This work is co-funded by the Centre National d'Études Spatiales (CNES) through A. Fossà PhD program, and made use of the CNES orbital propagation tools, including the PACE library.

References

- [1] ESA Space Debris Office, "ESA's Annual Space Environment Report," European Space Agency, Tech. Rep., May 2022. [Online]. Available: https://www.sdo.esoc.esa.int/environment_report/Space_Environment_Report_latest.pdf.
- [2] P. S. Laplace, *Memoires de l'Académie Royale des Sciences de Paris*. 1780.
- [3] C. F. Gauss, *Theoria Motus Corporum Coelestium in Sectionibus Conicis Solem Ambientium*. 1809.
- [4] P. R. Escobal, *Methods of orbit determination*. 1965.
- [5] R. Baker Jr and N. Jacobi Jr, "Preliminary orbit-determination method having no co-planar singularity," *Celestial Mechanics*, vol. 15, no. 2, pp. 137–160, 1977. DOI: [10.1007/BF01228460](https://doi.org/10.1007/BF01228460).
- [6] R. H. Gooding, "A new procedure for the solution of the classical problem of minimal orbit determination from three lines of sight," *Celestial Mechanics and Dynamical Astronomy*, vol. 66, no. 4, pp. 387–423, 1996. DOI: [10.1007/BF00049379](https://doi.org/10.1007/BF00049379).
- [7] R. R. Karimi and D. Mortari, "Initial orbit determination using multiple observations," *Celestial Mechanics and Dynamical Astronomy*, vol. 109, pp. 167–180, 2011. DOI: [10.1007/s10569-010-9321-3](https://doi.org/10.1007/s10569-010-9321-3).
- [8] D. Izzo, "Revisiting Lambert's problem," *Celestial Mechanics and Dynamical Astronomy*, vol. 121, no. 1, pp. 1–15, Jan. 2015, ISSN: 0923-2958. DOI: [10.1007/s10569-014-9587-y](https://doi.org/10.1007/s10569-014-9587-y). arXiv: [1403.2705](https://arxiv.org/abs/1403.2705). [Online]. Available: <http://link.springer.com/10.1007/s10569-014-9587-y>.
- [9] J. W. Gibbs, "On the determination of elliptic orbits from three complete observations," *Memoirs of the National Academy of Sciences*, vol. 4, no. 2, pp. 79–104, 1889.
- [10] S. Herrick, *Astrodynamics: Orbit Determination, Space Navigation, Celestial Mechanics*. 1971.
- [11] C. Yanez, F. Mercier, and J. Dolado Perez, "A novel initial orbit determination algorithm from Doppler and angular observations," in *Proc. 7th European Conference on Space Debris*, 2017, p. 8. [Online]. Available: <https://conference.sdo.esoc.esa.int/proceedings/sdc7/paper/337/SDC7-paper337.pdf>.
- [12] J. A. Christian and W. E. Parker, "Initial Orbit Determination from Bearing and Range-Rate Measurements Using the Orbital Hodograph," *Journal of Guidance, Control, and Dynamics*, vol. 44, no. 2, pp. 370–378, 2021. DOI: [10.2514/1.G005433](https://doi.org/10.2514/1.G005433).
- [13] A. Wittig, P. Di Lizia, R. Armellin, K. Makino, F. Bernelli-Zazzera, and M. Berz, "Propagation of large uncertainty sets in orbital dynamics by automatic domain splitting," *Celestial Mechanics and Dynamical Astronomy*, vol. 122, no. 3, pp. 239–261, Jul. 2015, ISSN: 15729478. DOI: [10.1007/s10569-015-9618-3](https://doi.org/10.1007/s10569-015-9618-3). [Online]. Available: <http://link.springer.com/10.1007/s10569-015-9618-3>.
- [14] L. Pirovano, D. A. Santeramo, R. Armellin, P. Di Lizia, and A. Wittig, "Probabilistic data association: the orbit set," *Celestial Mechanics and Dynamical Astronomy*, vol. 132, no. 15, p. 27, Feb. 2020, ISSN: 0923-2958. DOI: [10.1007/s10569-020-9951-z](https://doi.org/10.1007/s10569-020-9951-z). [Online]. Available: <http://link.springer.com/10.1007/s10569-020-9951-z>.
- [15] R. Armellin and P. Di Lizia, "Probabilistic Optical and Radar Initial Orbit Determination," *Journal of Guidance, Control, and Dynamics*, vol. 41, no. 1, pp. 101–118, 2018. DOI: [10.2514/1.G002217](https://doi.org/10.2514/1.G002217).

- [16] M. Losacco, R. Armellin, C. Yanez, L. Pirovano, S. Lizy-Destrez, and F. Sanfedino, “Robust initial orbit determination for surveillance doppler-only radars,” *IEEE Transactions on Aerospace and Electronic Systems*, pp. 1–12, 2023. DOI: [10.1109/TAES.2023.3249667](https://doi.org/10.1109/TAES.2023.3249667).
- [17] M. Berz, *Modern Map Methods in Particle Beam Physics*. 1999, p. 317, ISBN: 0120147505. [Online]. Available: <http://bt.pa.msu.edu/cgi-bin/display.pl?name=AIEP108book>.
- [18] M. Valli, R. Armellin, P. Di Lizia, and M. R. Lavagna, “Nonlinear Mapping of Uncertainties in Celestial Mechanics,” *Journal of Guidance, Control, and Dynamics*, vol. 36, no. 1, pp. 48–63, Jan. 2013, ISSN: 0731-5090. DOI: [10.2514/1.58068](https://doi.org/10.2514/1.58068). [Online]. Available: <https://arc.aiaa.org/doi/10.2514/1.58068>.
- [19] R. Armellin, D. Gondelach, and J. F. San Juan, “Multiple Revolution Perturbed Lambert Problem Solvers,” *Journal of Guidance, Control, and Dynamics*, vol. 41, no. 9, pp. 2019–2032, Sep. 2018, ISSN: 0731-5090. DOI: [10.2514/1.G003531](https://doi.org/10.2514/1.G003531). [Online]. Available: <https://arc.aiaa.org/doi/10.2514/1.G003531>.
- [20] D. A. Vallado, *Fundamentals of Astrodynamics and Applications*, 4th ed. 2013, p. 1106, ISBN: 978-1881883180.